research papers

Characterization of spatial coherence of synchrotron radiation with non-redundant arrays of apertures

P. Skopintsev,[a,b,c] A. Singer,[a‡] J. Bach,[d] L. Müller,[a] B. Beyersdorff,[d] S. Schleitzer,[a] O. Gorobtsov,[a,b] A. Shabalin,[a] R. P. Kurta,[a] D. Dzhigaev,[a,e] O. M. Yefanov,[a] L. Glaser,[a] A. Sakdinawat,[f] G. Grübel,[a,g] R. Frömter,[d] H. P. Oepen,[d] J. Viefhaus[a] and I. A. Vartanyants[a,e]*

[a]Deutsches Elektronen-Synchrotron DESY, Notkestrasse 85, D-22607 Hamburg, Germany, [b]National Research Center 'Kurchatov Institute', Kurchatov Square 1, 123182 Moscow, Russia, [c]Moscow Institute of Physics and Technology (State University), Dolgoprudny, Moscow Region 141700, Russia, [d]Universität Hamburg, Institut für Angewandte Physik, D-20355 Hamburg, Germany, [e]National Research Nuclear University, 'MEPhI', 115409 Moscow, Russia, [f]SLAC National Accelerator Laboratory, 2575 Sand Hill Road, Menlo Park, CA 94025-7015, USA, and [g]The Hamburg Center for Ultrafast Imaging, D-22761 Hamburg, Germany.
*E-mail: ivan.vartaniants@desy.de

A method to characterize the spatial coherence of soft X-ray radiation from a single diffraction pattern is presented. The technique is based on scattering from non-redundant arrays (NRAs) of slits and records the degree of spatial coherence at several relative separations from 1 to 15 µm, simultaneously. Using NRAs the spatial coherence of the X-ray beam at the XUV X-ray beamline P04 of the PETRA III synchrotron storage ring was measured as a function of different beam parameters. To verify the results obtained with the NRAs, additional Young's double-pinhole experiments were conducted and showed good agreement.

Keywords: coherence; interference; synchrotron X-ray sources.

1. Introduction

It is well established that the present-day third-generation synchrotrons are partially coherent sources (Winick, 1980; Attwood, 1999; Vartanyants & Singer, 2010). With the construction of these facilities, new research areas utilizing partial coherence of X-ray radiation have emerged. The most prominent experimental techniques are coherent X-ray diffractive imaging (CXDI) (Vartanyants *et al.*, 2010; Chapman & Nugent, 2010; Mancuso *et al.*, 2010), X-ray holography (Eisebitt *et al.*, 2004; Stickler *et al.*, 2010) and X-ray photon correlation spectroscopy (XPCS) (Grübel & Zontone, 2004). In CXDI, static real-space images of the sample are obtained by phase-retrieval techniques (Fienup, 1982), while correlation techniques are applied in XPCS to explore system dynamics (Goodman, 2007). The key feature of the methods utilizing the high degree of coherence is the interference of the field scattered by different parts of the sample under study. Hence, spatial coherence across the sample is essential and understanding the coherence proper-

ties of the beams at new-generation X-ray sources is of crucial importance for the scientific community. Moreover, a detailed knowledge of the beam coherence can be used to improve the resolution obtained in the CXDI phase retrieval (Whitehead *et al.*, 2009).

The Young's double-pinhole experiment is the most direct technique to map out the spatial coherence. The method has been successfully applied for soft X-ray synchrotron radiation (Chang *et al.*, 2000; Paterson *et al.*, 2001) and, recently, for free-electron lasers (FELs) (Singer *et al.*, 2008, 2012; Vartanyants *et al.*, 2011). However, a single double-pinhole experiment yields the spatial coherence at only one relative distance, the distance between the pinholes. To fully characterize the spatial coherence, several measurements at different pinhole separations are required. Other techniques have been implemented to measure the spatial coherence, such as X-ray grating interferometry (Pfeiffer *et al.*, 2005), phase-space tomography (Raymer *et al.*, 1994; Tran *et al.*, 2007), methods which utilize scattering on Brownian particles (Alaimo *et al.*, 2009), and measurements of the intensity correlations (Gluskin *et al.*, 1999; Yabashi *et al.*, 2001; Singer *et al.*, 2013). Similar to the double-pinhole experiment, the

‡ Present address: University of California, San Diego, CA 92093, USA.

aforementioned techniques require a number of measurements to fully determine the spatial coherence properties of the probing radiation.

Here we present a method to completely characterize the spatial coherence function of the soft X-ray radiation from a single diffraction pattern. This method utilizes a non-redundant array (NRA), *i.e.* a mask with multiple slits where each slit separation appears only once. Each pair of slits acts as a single Young's interferometer, and a measurement using an NRA can be considered as a series of double-pinhole interferograms acquired simultaneously. The signal from different slit pairs can be discriminated due to the uniqueness of each slit separation. This is in contrast to coherence measurements using a uniformly redundant array (URA), where each slit separation appears more than once (Lin *et al.*, 2003). The analysis of URA measurements is quite sensitive to the wavefront of the incident radiation (Vartanyants *et al.*, 2010), a limitation that is not present in NRA measurements. NRAs were previously used to measure spatial coherence of a He–Ne laser (Mejía & González, 2007; González & Mejía, 2011).

In this paper we demonstrate spatial coherence measurements performed at the XUV X-ray beamline P04 at PETRA III using NRA apertures.

2. Theory

In the theory of optical coherence, the statistical properties of the radiation, including spatial coherence, are described by correlation functions of the electric field. The mutual coherence function (MCF) is defined as (Goodman, 1985)

$$\Gamma(\mathbf{r}_1, \mathbf{r}_2; \tau) = \langle E^*(\mathbf{r}_1, t) \, E(\mathbf{r}_2, t + \tau) \rangle, \qquad (1)$$

where $E(\mathbf{r}_1, t)$ and $E(\mathbf{r}_2, t + \tau)$ are the field values at the positions $\mathbf{r}_1$ and $\mathbf{r}_2$ and times t and $t + \tau$, and $\langle \cdots \rangle$ is the ensemble average. The intensity $I(\mathbf{r})$ and complex degree of coherence $\gamma_{12}(\tau)$ can be readily obtained from the MCF,

$$I(\mathbf{r}) = \Gamma(\mathbf{r}, \mathbf{r}; 0), \qquad \gamma_{12}(\tau) = \frac{\Gamma(\mathbf{r}_1, \mathbf{r}_2; \tau)}{\left[I(\mathbf{r}_1) \, I(\mathbf{r}_2)\right]^{1/2}}. \qquad (2)$$

If the time delay τ is much smaller than the coherence time τ_c, $\gamma_{12}(\tau)$ can be well approximated by the complex coherence factor (CCF) $\gamma_{12} = \gamma_{12}(0)$ (Goodman, 1985) that does not depend on the time delay τ.

In the frame of the Gaussian Schell-model, which in most cases provides sufficient description of synchrotron radiation (Vartanyants & Singer, 2010), the intensity profile and the CCF are both Gaussian functions. The beam size in this model is characterized by its root mean square (r.m.s.) width σ of the intensity and the transverse coherence length l_c can be defined as the r.m.s. width of $|\gamma_{12}|$. To characterize the transverse coherence by one number, the global degree of coherence can be introduced (Saldin *et al.*, 2008; Vartanyants & Singer, 2010),

$$\zeta = (l_c/\sigma)\left[4 + (l_c/\sigma)^2\right]^{-1/2}. \qquad (3)$$

To measure the CCF of the radiation an arrangement of apertures can be used as a scattering object. The correlations between the field scattered at the apertures and propagated to the detection plane can be recorded as intensity modulations or interference fringes. For the narrow bandwidth radiation, the far-field diffraction pattern $I(\mathbf{q})$ of N identical apertures can be expressed in the following way (Mejía & González, 2007; González & Mejía, 2011),

$$I(\mathbf{q}) = I_S(\mathbf{q})\left\{C_0 + \sum_{i \neq j}^N C_{ij} \exp\left[i(\mathbf{q} \cdot \mathbf{d}_{ij} + \alpha_{ij})\right]\right\}, \qquad (4)$$

where coefficients C_0 and C_{ij} are defined as

$$C_0 = \sum_i I_i, \qquad C_{ij} = |\gamma_{ij}| (I_i I_j)^{1/2}. \qquad (5)$$

Here I_i is the intensity incident on the aperture i,[1] $|\gamma_{ij}|$ is the modulus of the CCF at the aperture separation vector $\mathbf{d}_{ij} = -\mathbf{d}_{ji}$, $\alpha_{ij} = -\alpha_{ji}$ is the relative phase, $I_S(\mathbf{q})$ is the intensity distribution on the detector due to beam diffraction on a single aperture, and $\mathbf{q}$ is the momentum transfer vector. If the aperture has the form of a pinhole, then $I_S(\mathbf{q})$ is the well known Airy pattern. For a rectangular slit, $I_S(\mathbf{q})$ has the shape of a squared sinc function. An example of the intensity distribution $I(\mathbf{q})$ for diffraction on six and two slits is shown in Figs. 1(*a*) and 1(*c*).

The interference pattern in equation (4) can be conveniently analyzed using the Fourier transform $\hat{I}(\Delta \mathbf{x})$ of $I(\mathbf{q})$, which for N apertures is given by (Bartels *et al.*, 2002; Mejía & González, 2007; González & Mejía, 2011)

$$\hat{I}(\Delta \mathbf{x}) = \hat{I}_S(\Delta \mathbf{x}) \otimes \left\{C_0 \delta(\Delta \mathbf{x}) \right.$$
$$\left. + \sum_{i \neq j}^N C_{ij}\left[\exp(i\alpha_{ij}) \, \delta(\Delta \mathbf{x} - \mathbf{d}_{ij})\right]\right\}, \qquad (6)$$

where $\delta(\Delta \mathbf{x})$ is the Dirac delta function, $\hat{I}_S(\Delta \mathbf{x})$ is the Fourier transform of $I_S(\mathbf{q})$, the symbol $\otimes$ denotes the convolution, and $\Delta \mathbf{x}$ denotes the relative distance. It is clear from expression (6) that the peak maximum at each peak separation $\mathbf{d}_{ij}$ is given by coefficients C_{ij}. If the intensities I_i incident on the apertures are known, the CCF can be readily obtained from equation (5) as

$$|\gamma_{ij}| = C_{ij}/(I_i I_j)^{1/2}, \qquad (7)$$

for all $\mathbf{d}_{ij}$. An NRA with N slits shows $N(N-1) + 1$ individual peaks in the Fourier transform $\hat{I}(\Delta \mathbf{x})$ of the measured intensity $I(\mathbf{q})$, whereas each peak corresponds to interference between a unique combination of two slits. According to equation (7), each peak in equation (6) corresponds to a unique value of $|\gamma_{ij}|$. Typical distributions $\hat{I}(\Delta \mathbf{x})$ with 31 and 3 peaks, corresponding to six and two slit apertures, are shown in Figs. 1(*b*) and 1(*d*).

It is clear that the outcome of the measurement strongly depends on the design of the NRA. To optimize the NRA

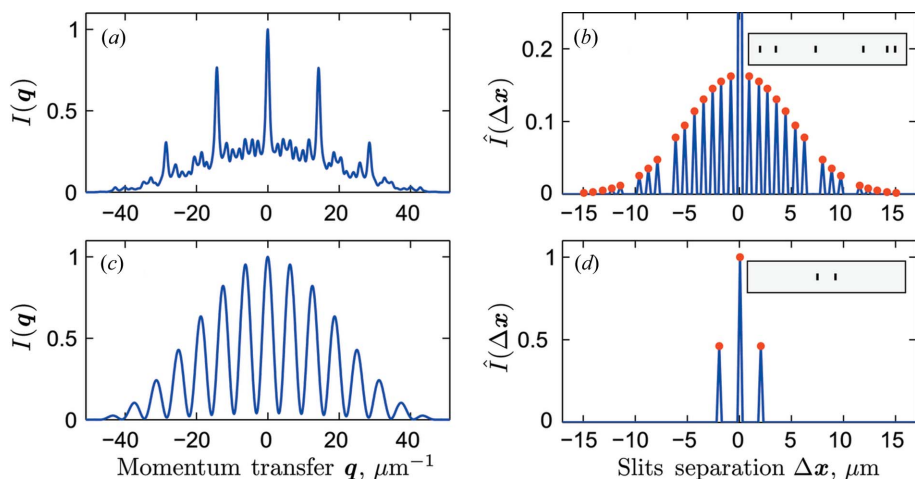[1] Here we assume that the incident intensity is constant across a single aperture.

Figure 1
(a, c) Simulated diffraction patterns $I(q)$ from NRAs of six (a) and two (c) slits. (b, d) Fourier transform $\hat{I}(\Delta x)$ of corresponding diffraction patterns from six (b) and two (d) slits. Red points in (b, d) denote the central and satellite peaks' maxima C_0 and C_{ij}, respectively. The insets in (b) and (d) show the slits' relative positions used in simulations. The radiation was uniformly distributed in the slits and had a coherence length of $l_c = 5$ μm.

structure one possibility would be to find a uniform spatial distribution of the peaks. It can be shown that such an ideal NRA with a uniform distribution of the peaks can only be achieved with four slits (Dollas *et al.*, 1998). For more than four slits the peaks can be uniformly distributed, but some of them will be missing. However, it is still possible to find an arrangement of N slits with as few missing peaks as possible. In this work we designed NRAs using a so-called Golomb ruler[2] that has integer marks with a distinct distance between every two marks.

3. Experiment

The coherence measurements were performed at the Variable Polarization XUV beamline P04 (Viefhaus *et al.*, 2013) of the PETRA III synchrotron radiation source at DESY in Hamburg during commissioning. The beamline set-up is schematically presented in Fig. 2. A 5 m APPLE-II type
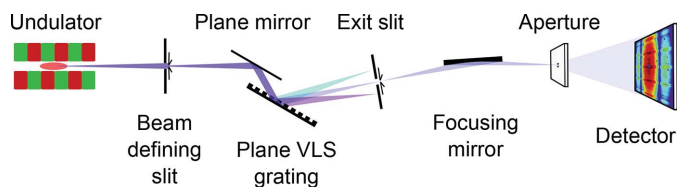

Figure 2
Experimental set-up. Synchrotron radiation is generated by a 5 m APPLE-II type undulator and is transmitted through the beamline including a beam-defining slit, monochromator comprised of a VLS plane grating and pair of plane mirrors, exit slit, focusing mirror and collimating mirror. The beam is focused on the apertures by the focusing mirror and forms a diffraction pattern on the CCD detector positioned in the far-field. The horizontal plane mirror and the collimating mirror are not shown in the figure.

helical undulator with 72 magnetic periods was tuned to deliver 400 eV (wavelength λ = 3.1 nm) photons. The beam further propagated to the end-station through several optical elements, including a beam-defining slit (27 m downstream from the undulator), horizontal plane mirror (35 m) and vertical plane mirror together with a plane varied-line-spacing (VLS) grating (46 m). The VLS grating focused the beam at the exit slit (71 m). An elliptical mirror (78.5 m) focused the beam vertically to the sample position (81 m). Horizontally the beam was collimated by a cylindrical mirror (79.1 m) and defined by a slit in front of the sample. All mirrors were designed to accept 6σ r.m.s. of the beam size.

NRAs and double pinholes were manufactured in an opaque screen [see Vartanyants *et al.* (2011) for a detailed description of the manufacturing process] and were used to map out the transverse coherence of the beam. The distance between individual slits in the NRA aperture was varying between 1 μm and 15 μm. The slits were positioned at -7.5 μm, -6.62 μm, -3.97 μm, 1.32 μm, 5.74 μm and 7.5 μm and each slit was 0.8 μm × 0.25 μm in size with the smaller size being along the NRA direction [see the inset in Fig. 1(b)]. Double-pinhole apertures had a separation of between 2 μm and 15 μm, whereas the pinhole size varied between 0.34 μm and 0.5 μm. The apertures were mounted on a piezo-positioner stage with a travel range of up to 20 mm. Finally, the interference patterns were recorded by a Spectral Instruments 1100S charge-coupled device (CCD) with 4096 × 4112 pixels, each 15 μm × 15 μm in size. The dynamic range of the detector was 10^4. The typical exposure time for one frame of the diffraction patterns was 60 s for double pinholes and 12 s for NRA apertures. Each diffraction pattern was an accumulation of three exposures for double pinholes and 30 exposures for NRAs. The detector was positioned 0.8 m downstream of the sample and a round beamstop, 700 μm in diameter, protected the detector from the direct beam.

The transverse coherence and the intensity profile in the vertical direction were measured for different beamline parameters, including the monochromator exit slit size, beam-defining slit size downstream of the undulator, and the photon energy transmitted through the monochromator. The monochromator exit slit width was varied between 40 μm and 230 μm, while the monochromator was tuned to an energy of 400 eV (maximum flux) and the beam-defining slit was opened to 4.7 mm. In this initial stage of beamline commissioning the photon energy resolution was the same for both exit slit openings, resulting in a bandwidth of about 0.5 eV.[3] This gave

---

[2] For a list of all currently available optimal Golomb rulers, see Lam & Sarwate (1988) (see also Wikipedia, 2014).

[3] At this very early stage of commissioning the grating did not yet deliver the designed resolving power ($E/\Delta E > 10000$).
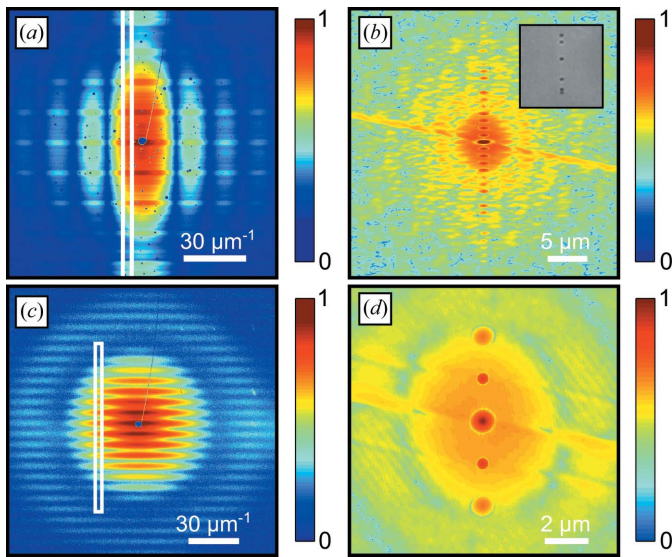
Figure 3
(a, c) Diffraction patterns from NRA apertures with six slits (a) and double pinholes with a separation of 2 µm (c) measured at 400 eV photon energy and monochromator exit slits size D_{es} = 230 µm. (b, d) Fourier transforms of the diffraction patterns in (a, c). All figures are displayed on a logarithmic scale. White rectangles in (a) and (c) indicate regions which were used for the analysis. An optical microscope image of the NRA sample is shown in the inset of (b).

us an estimate of the temporal coherence length $l_t = c\tau_c$ that was l_t = 1.6 µm in the conditions of our experiment. For the rest of the measurements the exit slit size was fixed to the value D_{es} = 230 µm and the beam-defining slit size D_{ds} was chosen to be 4.7 mm, 1.7 mm and 0.8 mm. These slits correspond to a relative transmitted flux of 1, 0.5 and 0.25, respectively. For each beam-defining slit width we measured the transverse coherence at photon energies of 396.5 eV, 400 eV and 403 eV, which were selected by the monochromator for a fixed undulator gap. At 400 eV the maximum

flux was observed, whereas at 396.5 eV and 403 eV the flux was reduced by a factor of two.

Six-slits NRA diffraction patterns were collected for all beamline parameters. Additionally, double-pinhole interferograms were measured for the case of exit slit widths of 40 µm and 230 µm. A sufficient sampling of interference fringes was obtained in all cases with at least 11 pixels per fringe for a 15 µm aperture separation.

4. Results and discussion

Typical recorded and dark-field-corrected diffraction patterns of six-slits NRA and double pinholes are shown in Figs. 3(a) and 3(c), respectively. Both interferograms were measured at 400 eV photon energy, 4.7 mm beam-defining slits opening, and monochromator exit slit width D_{es} = 230 µm. Peaks corresponding to the aperture interference are clearly visible in the Fourier transforms of both diffraction patterns presented in Figs. 3(b) and 3(d). It is interesting to note that in these Fourier transforms of diffraction patterns the contribution of the higher harmonic radiation at 800 eV photon energy transmitted through the monochromator reveals itself in additional peaks at larger distances visible in Fig. 3(d). Their height is less than 8% compared with the 400 eV peaks located closer to the central peak. The randomly distributed black spots in Fig. 3(a) are due to contaminations formed at the surface of the detector at the end of the experiment. The streak visible in Figs. 3(b) and 3(d) is due to a shadow of the beamstop holder visible in Figs. 3(a) and 3(c).

The peak heights C_0 and C_{ij} for both NRA and double-pinholes diffraction patterns were retrieved from the Fourier transform of a vertical line scan, obtained by averaging 31 pixel-wide regions marked by the white rectangle in Figs. 3(a) and Fig. 3(c). Corresponding line scans of diffraction patterns and their Fourier transforms are shown in Fig. 4. In these regions, high harmonic 800 eV radiation has a minimum
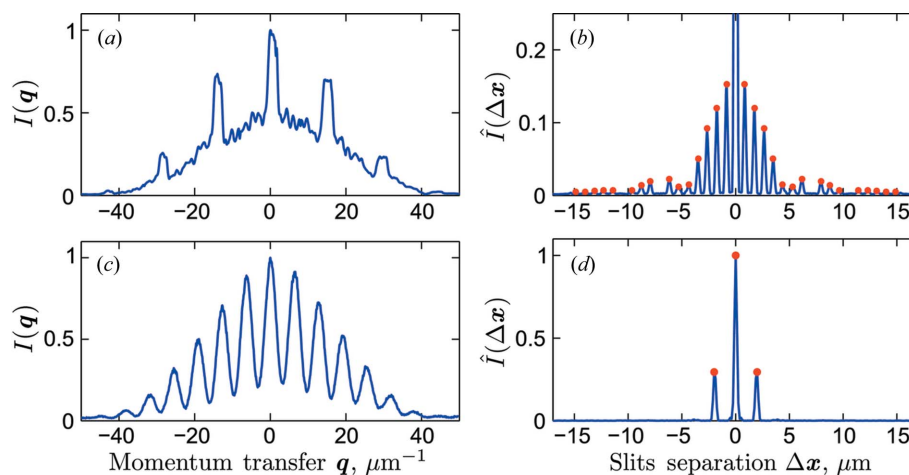

Figure 4
(a, c) Line scans of diffraction patterns $I(q)$ in the vertical direction from the NRA of six slits (a) and double pinholes (c) obtained by averaging the white regions shown in Figs. 3(a) and 3(b), respectively. (b, d) Fourier transforms $\hat{I}(\Delta x)$ of the corresponding line scans from the NRA (b) and double pinholes (d). Red points in (b, d) denote the central and satellite peaks maxima C_0 and C_{ij}.
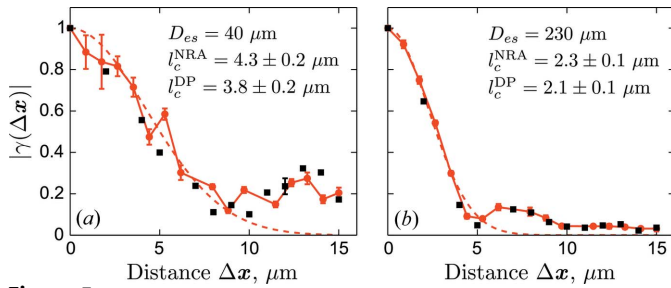
Figure 5
Modulus of the CCF $|\gamma(\Delta x)|$ for 400 eV synchrotron radiation and monochromator exit slit widths of $D_{es} = 40$ μm (a) and 230 μm (b). Red circles, connected with red lines, represent values of the CCF measured by the NRA method and black squares correspond to the values determined by the double pinholes. Gaussian fits for the CCF values obtained with NRAs are shown by dashed red lines.

Table 1
Coherence length l_c^{NRA}, l_c^{DP} and normalized degree of coherence ζ^{NRA}, ζ^{DP} measured with NRA and double pinholes (DP) for different exit slit widths of the monochromator D_{es}.

The beam had a FWHM of 11 ± 1 μm in the case of $D_{es} = 40$ μm and 42 ± 2 μm in the case of $D_{es} = 230$ μm. The photon energy was 400 eV and the beam-defining slit was set to 4.7 mm.

Parameter	Exit slit D_{es}	
	40 μm	230 μm
l_c^{NRA} (μm)	4.3 ± 0.2	2.4 ± 0.1
l_c^{DP} (μm)	3.8 ± 0.2	2.1 ± 0.1
ζ^{NRA}	0.41 ± 0.04	0.06 ± 0.01
ζ^{DP}	0.38 ± 0.03	0.06 ± 0.01

contribution and temporal coherence effects can be neglected due to small scattering angles.[4]

To determine the intensity distribution in the focus of the beam, the beam profile scans were performed by the double pinholes with a separation of 15 μm. A position uncertainty of ± 1 μm was observed during the experiment. Each profile scan was fitted with two Gaussian functions with the same width and 15 μm separation. The beam FWHM was determined to be in the range from 10 μm to 12 μm for the exit slits size $D_{es} = 40$ μm and in the range from 40 μm to 44 μm for $D_{es} = 230$ μm. The beam size appeared to be independent of the photon energy and the beam-defining slits width. To define the values of the incident intensities I_i at the apertures we assumed that the beam has a Gaussian shape, and is positioned in the center of the NRA aperture with FWHM of 11 μm and 42 μm for the exit slits D_{es} of 40 μm and 230 μm, respectively.

Finally, the peak heights C_{ij} and the measured incident intensity profiles I_i were used in equation (7) to determine the modulus of the CCF $|\gamma_{ij}|$. The result from the NRA measurements is presented in Fig. 5 together with the double-pinhole measurements. It is important to note that the results obtained with the NRA of apertures are in excellent agreement with a well established measurement using double pinholes, whereas the measurement time is reduced by an order of magnitude to acquire the same information.

The error bars of the CCF were estimated using a set of incident intensities having FWHM and center of the beam position uncertainty within the error margins given by the intensity measurements. Using equation (7), $|\gamma_{ij}|$ was calculated from each intensity profile and the uncertainty of $|\gamma_{ij}|$ was found from the deviation of these values. The errors are comparably large when the beam size is small relative to the NRA size (that was 15 μm in our experiment), as in the case of 40 μm exit slit opening.[5] When the FWHM of the focused

beam was larger than the total NRA size, as in the case of the 230 μm exit slit opening, practically no errors occurred (see Fig. 5b).

To estimate the spatial coherence length l_c, the values of the modulus of the CCF $|\gamma(\Delta x)|$ were approximated by a Gaussian $\exp[-\Delta x^2/(2l_c^2)]$. Results of our evaluation for the NRA as well as for the double pinholes are presented in Table 1. The values of the global degree of coherence ζ [see equation (3)] are also given in the same table. These results demonstrate an excellent agreement between both methods.

Finally, we present spatial coherence measurements performed with NRA apertures for the cases of 396.5 eV, 400 eV and 403 eV beam energies as well as 4.7 mm, 1.7 mm and 0.8 mm beam-defining slit width. In all cases the monochromator exit slit width was set to $D_{es} = 230$ μm. The results of these measurements are presented in Fig. 6. The transverse coherence length l_c for all curves was determined by the Gaussian fit, as before, and the result is summarized in Table 2.

As expected, the coherence length l_c is inversely proportional to the beam-defining slit width. The slit widths were chosen such that the transmitted intensity drops by a factor of two in each step. Interestingly, the normalized degree of coherence ζ increases by about a factor of two in each step. This means that in the range accessed in our experiment the beam-defining slit cuts out the coherent part of the beam and almost no coherent flux is lost. For the blue-shifted beam (403 eV) this relation does not hold due to a high value of the normalized degree of coherence (Singer & Vartanyants, 2011).

We also observed a variation of the transverse coherence length as a function of the monochromator tuning energy. The energies were chosen such that the maximum flux at 400 eV was reduced by a factor of two for both energies 403 eV and 396.5 eV. For the largest beam-defining slit (4.7 mm) the coherence length increases by 25% when the monochromator is detuned to 403 eV. However, unlike in the case of the beam-defining slit the coherent flux is reduced. Interestingly, the functional form appears to be closer to a Gaussian function for the blue-shifted radiation. We want to note here that it is the power of the method here that allows these fine details of the coherence function to be recorded. For an energy of 396.5 eV
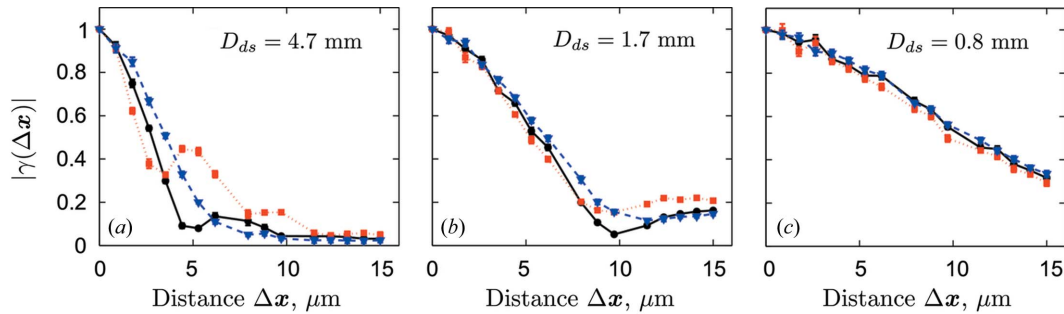
---

[4] Our estimates show that the maximum optical path length difference l is about $l = 0.4$ μm in the region chosen for the analysis. This is smaller than the temporal coherence length $l_t = 1.6$ μm and it means that our assumption $\tau < \tau_c$ is well satisfied in this region.

[5] In fact, for the exit slit width of 40 μm the incident beam was smaller than the NRA size and we additionally had to find the position of the incident beam relative to the center of the NRA using additional constrains, such as avoiding values of $|\gamma_{ij}|$ larger than 1, smallest uncertainties and smoothness of the CCF.

Figure 6
Modulus of the CCF $|\gamma(\Delta x)|$ measured for an exit slit width of D_{es} = 230 µm and beam-defining slit widths of D_{ds} = 4.7 mm (*a*), 1.7 mm (*b*) and 0.8 mm (*c*). Measurements performed at 396.5 eV (red squares), 400 eV (blue triangles) and 403 eV (black circles) are presented.

Table 2
Coherence length l_c and normalized degree of coherence ζ for different photon energies and beam-defining slit size D_{ds} obtained as a result of the analysis of data presented in Fig. 6.

The monochromator exit slits were fixed to D_{es} = 230 µm.

Energy (eV)	Parameter	Beam-defining slit D_{ds}		
		4.7 mm	1.7 mm	0.8 mm
396.5	l_c (µm)	1.9 ± 0.1	4.4 ± 0.1	8.8 ± 0.3
	ζ	0.05 ± 0.01	0.12 ± 0.01	0.24 ± 0.01
400	l_c (µm)	2.4 ± 0.1	4.6 ± 0.1	9.2 ± 0.2
	ζ	0.06 ± 0.01	0.13 ± 0.01	0.25 ± 0.01
403	l_c (µm)	3.0 ± 0.1	5.1 ± 0.1	9.4 ± 0.2
	ζ	0.08 ± 0.01	0.14 ± 0.01	0.25 ± 0.01

the transverse coherence is worse.[6] The energy dependence of the transverse coherence is significantly smaller (about 5%) for the smallest beam-defining slit.

5. Conclusions and outlook

In conclusion, a non-redundant array of apertures provides a fast and effective way to determine the transverse coherence function of the undulator radiation in one direction. We showed that in this method a single diffraction pattern is sufficient to find the degree of coherence of X-ray radiation at several relative distances simultaneously. The results obtained with NRA apertures concord well with the values determined using Young's double pinholes, whereas the measurement time was reduced significantly. The dependence of spatial coherence on different parameters was explored. The transverse coherence length shows an inverse proportional dependence on both the width of the beam-defining slit and the exit slit. We also observed that the spatial coherence improves if the monochromator is offset to larger energies (blue-shifted) and it is decreased for smaller energies (red-shifted). We anticipate that the method presented here will be a useful procedure for XUV and soft X-ray beam calibration prior to any experiment utilizing spatial coherence. A natural extension of this method will be to obtain transverse coher-

ence properties of the beam in two dimensions simultaneously. This can be done, for example, by designing two-dimensional NRA apertures as proposed by González & Mejía (2011). We also foresee that in future the NRA method could become a viable tool for single-pulse coherence characterization measurements at free-electron lasers (Singer *et al.*, 2008, 2012; Vartanyants *et al.*, 2010, 2011).

References

Alaimo, M. D., Potenza, M. A. C., Manfredda, M., Geloni, G., Sztucki, M., Narayanan, T. & Giglio, M. (2009). *Phys. Rev. Lett.* **103**, 194805.
Attwood, D. (1999). *Soft X-rays and Extreme Ultraviolet Radiation*. Cambridge University Press.
Bartels, R. A., Paul, A., Green, H., Kapteyn, H. C., Murnane, M. M., Backus, S., Christov, I. P., Liu, Y., Attwood, D. & Jacobsen, C. (2002). *Science*, **297**, 376–378.
Chang, C., Naulleau, P., Anderson, E. & Attwood, D. (2000). *Opt. Commun.* **182**, 25–34.
Chapman, H. N. & Nugent, K. A. (2010). *Nat. Photon.* **4**, 833–839.
Dollas, A., Rankin, W. T. & McCracken, D. (1998). *IEEE Trans. Inf. Theory*, **44**, 379–382.
Eisebitt, S., Lüning, J., Schlotter, W. F., Lörgen, M., Hellwig, O., Eberhardt, W. & Stöhr, J. (2004). *Nature (London)*, **432**, 885–888.
Fienup, J. R. (1982). *Appl. Opt.* **21**, 2758–2769.
Gluskin, E., Alp, E. E., McNulty, I., Sturhahn, W. & Sutter, J. (1999). *J. Synchrotron Rad.* **6**, 1065–1066.
González, A. I. & Mejía, Y. (2011). *J. Opt. Soc. Am. A*, **28**, 1107–1113.
Goodman, J. W. (1985). *Statistical Optics*. New York: Wiley.
Goodman, J. W. (2007). *Speckle Phenomena in Optics*. Greenwood Village: Roberts.

[6] This effect could be due to the fact that on the higher-energy side of the undulator peak the collimation of the undulator cone is better than towards the lower-energy side where at even lower energies an intensity minimum is observed on-axis, resulting in a non-optimal beam path.

Grübel, G. & Zontone, F. (2004). *J. Alloys Compd.* **362**, 3–11.

Lam, A. W. & Sarwate, D. V. (1988). *IEEE Trans. Commun.* **36**, 380–382.

Lin, J. J. A., Paterson, D., Peele, A. G., McMahon, P. J., Chantler, C. T., Nugent, K. A., Lai, B., Moldovan, N., Cai, Z., Mancini, D. C. & McNulty, I. (2003). *Phys. Rev. Lett.* **90**, 074801.

Mancuso, A. P. *et al.* (2010). *New J. Phys.* **12**, 035003.

Mejía, Y. & González, A. I. (2007). *Opt. Commun.* **273**, 428–434.

Paterson, D., Allman, B. E., McMahon, P. J., Lin, J., Moldovan, N., Nugent, K. A., McNulty, I., Chantler, C. T., Retsch, C. C., Irving, T. H. K. & Mancini, D. C. (2001). *Opt. Commun.* **195**, 79–84.

Pfeiffer, F., Bunk, O., Schulze-Briese, C., Diaz, A., Weitkamp, T., David, C., van der Veen, J. F., Vartanyants, I. & Robinson, I. K. (2005). *Phys. Rev. Lett.* **94**, 164801.

Raymer, M. G., Beck, M. & McAlister, D. (1994). *Phys. Rev. Lett.* **72**, 1137–1140.

Saldin, E. L., Schneidmiller, E. A. & Yurkov, M. V. (2008). *Opt. Commun.* **281**, 1179–1188.

Singer, A. *et al.* (2012). *Opt. Express*, **20**, 17480–17495.

Singer, A., Lorenz, U., Sorgenfrei, F., Gerasimova, N., Gulden, J., Yefanov, O. M., Kurta, R. P., Shabalin, A., Dronyak, R., Treusch, R., Kocharyan, V., Weckert, E., Wurth, W. & Vartanyants, I. A. (2013). *Phys. Rev. Lett.* **111**, 034802.

Singer, A. & Vartanyants, I. A. (2011). *Proc. SPIE*, **8141**, 814106.

Singer, A., Vartanyants, I. A., Kuhlmann, M., Duesterer, S., Treusch, R. & Feldhaus, J. (2008). *Phys. Rev. Lett.* **101**, 254801.

Stickler, D., Frömter, R., Stillrich, H., Menk, C., Tieg, C., Streit-Nierobisch, S., Sprung, M., Gutt, C., Stadler, L.-M., Leupold, O., Grübel, G. & Oepen, H. P. (2010). *Appl. Phys. Lett.* **96**, 042501.

Tran, C. Q., Williams, G. J., Roberts, A., Flewett, S., Peele, A. G., Paterson, D., de Jonge, M. D. & Nugent, K. A. (2007). *Phys. Rev. Lett.* **98**, 224801.

Vartanyants, I. A., Mancuso, A. P., Singer, A., Yefanov, O. M. & Gulden, J. (2010). *J. Phys. B: At. Mol. Opt. Phys.* **43**, 194016.

Vartanyants, I. A. & Singer, A. (2010). *New J. Phys.* **12**, 035004.

Vartanyants, I. A. *et al.* (2011). *Phys. Rev. Lett.* **107**, 144801.

Viefhaus, J., Scholz, F., Deinert, S., Glaser, L., Ilchen, M., Seltmann, J., Walter, P. & Siewert, F. (2013). *Nucl. Instrum. Methods Phys. Res. A*, **710**, 151–154.

Whitehead, L. W., Williams, G. J., Quiney, H. M., Vine, D. J., Dilanian, R. A., Flewett, S., Nugent, K. A., Peele, A. G., Balaur, E. & McNulty, I. (2009). *Phys. Rev. Lett.* **103**, 243902.

Wikipedia (2014). Golomb ruler. Wikipedia, the Free Encyclopedia. [Online; accessed 19 January 2014.]

Winick, H. (1980). *Synchrotron Radiation Research*, edited by H. Winick and S. Doniach. New York/London: Plenum.

Yabashi, M., Tamasaku, K. & Ishikawa, T. (2001). *Phys. Rev. Lett.* **87**, 140801.